Tunable Interband Transitions in Twisted *h*-BN/Graphene Heterostructures

Bingyao Liu,[1,2,3] Yu-Tian Zhang [ORCID],[4] Ruixi Qiao,[5] Ruochen Shi [ORCID],[1] Yuehui Li,[1] Quanlin Guo,[6] Jiade Li,[4,7] Xiaomei Li,[1] Li Wang,[7] Jiajie Qi,[6] Shixuan Du,[4,8] Xinguo Ren [ORCID],[7] Kaihui Liu,[6,8,9,*] Peng Gao [ORCID],[1,2,3,9,10,†] and Yu-Yang Zhang [ORCID][4,‡]

[1]*Electron Microscopy Laboratory, and International Center for Quantum Materials, School of Physics, Peking University, Beijing 100871, China*
[2]*Beijing Graphene Institute (BGI), Beijing 100095, China*
[3]*Academy for Advanced Interdisciplinary Studies, Peking University, Beijing 100871, China*
[4]*University of Chinese Academy of Sciences and Institute of Physics, Chinese Academy of Sciences, Beijing 100049, China*
[5]*Institute for Frontier Science, Nanjing University of Aeronautics and Astronautics, Nanjing 210016, China*
[6]*State Key Laboratory for Mesoscopic Physics, Frontiers Science Center for Nano-optoelectronics, School of Physics, Peking University, Beijing 100871, China*
[7]*Beijing National Laboratory for Condensed Matter Physics, Institute of Physics, Chinese Academy of Sciences, Beijing 100190, China*
[8]*Songshan Lake Materials Laboratory, Dongguan, Guangdong 523808, China*
[9]*Collaborative Innovation Center of Quantum Matter, Beijing 100871, China*
[10]*Interdisciplinary Institute of Light-Element Quantum Materials and Research Center for Light-Element Advanced Materials, Peking University, Beijing 100871, China*

In twisted *h*-BN/graphene heterostructures, the complex electronic properties of the fast-traveling electron gas in graphene are usually considered to be fully revealed. However, the randomly twisted heterostructures may also have unexpected transition behaviors, which may influence the device performance. Here, we study the twist-angle-dependent coupling effects of *h*-BN/graphene heterostructures using monochromatic electron energy loss spectroscopy. We find that the moiré potentials alter the band structure of graphene, resulting in a redshift of the intralayer transition at the M point, which becomes more pronounced up to 0.22 eV with increasing twist angle. Furthermore, the twisting of the Brillouin zone of *h*-BN relative to the graphene M point leads to tunable vertical transition energies in the range of 5.1–5.6 eV. Our findings indicate that twist-coupling effects of van der Waals heterostructures should be carefully considered in device fabrications, and the continuously tunable interband transitions through the twist angle can serve as a new degree of freedom to design optoelectrical devices.

Two-dimensional (2D) materials have various electronic structures and can be artificially assembled, drawing great attention since the first exfoliation of graphene [1]. When stacked together, there will be no strict limitation in lattice matching during heterostructure assembling due to the van der Waals interaction in 2D materials [2], bringing possibilities for many complex structures [3–5]. The twist angle between these stacked 2D layers also supplies a new degree of freedom to perform band gap engineering [6–8]. The tunable interfacial interaction offers platforms to study many interesting phenomena, e.g., the continuously tunable van Hove singularities (vHS) [9–13] and subsequent superconductivity [14] in twisted bilayer graphene, second-generation Dirac cones in hexagonal boron nitride (*h*-BN)/graphene heterostructures [15,16], and moiré excitons in twisted transition-metal-dichalcogenides [17,18].

In van der Waals heterostructure optoelectronic devices, *h*-BN and graphene are often used as dielectric encapsulation layers [19] and electrodes [20,21], respectively. *h*-BN usually serves as a substrate or encapsulation layer to hold other fragile 2D materials or protect them from

exposure to the environment and avoid oxidation or contamination due to its stability and dangling bond-free properties [17,18,22,23], while it has a minor influence on the intrinsic performance of the devices due to its large band gap [24]. As a 2D semimetal material, graphene has a flat surface and zero band gap [25,26] and is thus suitable for electrical contact in 2D devices [27]. However, the contact of graphene and *h*-BN creates 2D heterointerfaces, in which the interfacial moiré potential between them may influence the band structure [28]. Especially at some specific twist angles, the overlapped bands of the stacked layers created new vHS without symmetry protection, and some unexpected interlayer vertical transitions may also influence the electrical and optical properties of the devices.

Herein, by using scanning transmission electron microscopy–electron energy loss spectroscopy (STEM-EELS) and first-principle calculations, we find that the interband transition behavior in *h*-BN/graphene van der Waals heterostructures exhibits a strong twist-angle dependence. The moiré potentials add interference to the energy bands
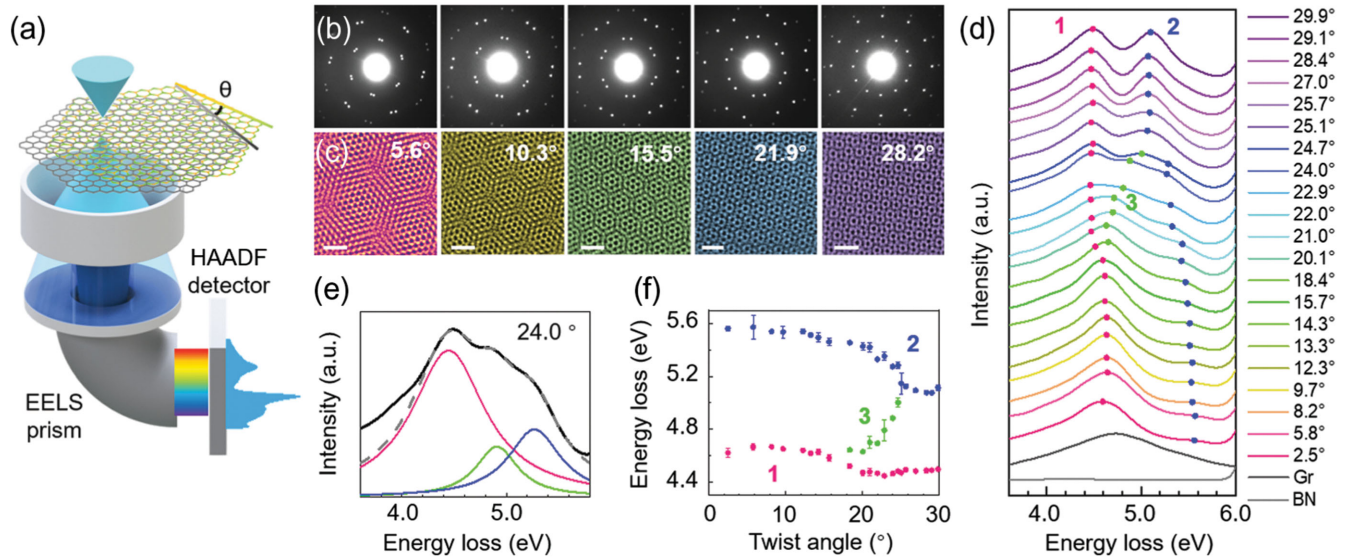
FIG. 1. Twist-angle-resolved STEM-EELS of h-BN/graphene (Gr) vertical heterostructures. (a) Schematic of the STEM-EELS measurement. (b),(c) Diffraction patterns (b) and HAADF images (c) of h-BN/Gr with twist angles of 5.6°, 10.3°, 15.5°, 21.9°, and 28.2°. Scale bars: 1 nm. (d) EELS spectra of monolayer Gr, monolayer h-BN, and h-BN/Gr heterostructures with different twist angles. Three peaks labeled as first, second, and third transitions are found in these spectra. (e) An example showing the process of extracting the peak positions for the 24.0° twist h-BN/Gr signal by Gaussian fitting. The pink, blue, and green peaks correspond to the fitted first, second, and third transitions, respectively. The dashed gray line indicates the sum of three fitted peaks. (f) Extracted transition energies. The error bars are calculated by multiple measurements.

of graphene, making the intralayer transition redshift as the twist angle increases. Meanwhile, since the reciprocal lattices of h-BN and graphene also twist concurrently as their lattices twist in real space, such a twisting of the h-BN Brillouin zone (BZ) projected onto the graphene M point leads to tunable vertical transition energies. Our study reveals the angle-dependent coupling behavior between h-BN and graphene, indicating that the coupling effects in 2D devices should be carefully considered to prevent unexpected transitions and/or transition energy shifts. Moreover, the revealed twist-angle-related transition behavior in twisted h-BN/graphene enables tunable intralayer and interlayer transition energies, creating opportunities for the fabrication of new 2D optoelectrical devices [27,29] with artificially specified wavelengths.

We used chemical-vapor-deposition-synthesized graphene and h-BN monolayers to assemble vertical heterostructures, which were subsequently transferred onto TEM grids for characterization. A schematic of the STEM-EELS measurement is shown in Fig. 1(a). High-angle annular dark field (HAADF) images and EELS spectra were recorded simultaneously. The former, together with the selected area electron diffraction (SAED) patterns, were employed to determine the twist angles. Figure 1(b) shows five typical SAED patterns with twist angles of 5.6°, 10.3°, 15.5°, 21.9°, and 28.2°, where two sets of sixfold symmetry diffraction patterns corresponding to graphene and h-BN are rotated from each other and show slightly different lattice constants (the lattice constant of h-BN is ∼1.8% larger than that of

graphene [30]). The HAADF images taken in corresponding areas show different moiré periods [Fig. 1(c)], which fit well with the results calculated from the twist angles extracted from SAED (Supplemental Material [31] Fig. S1). The typical EELS spectra of twist-angle-dependent transitions in h-BN/graphene vertical heterostructures are shown in Fig. 1(d). The overlaid peaks are fitted by Gaussian peaks; e.g., a 24.0° twist case is shown in Fig. 1(e). The extracted peak positions are plotted in Fig. 1(f). The corresponding twist angle determined SAED patterns are shown in Supplemental Material Fig. S2 [31]. Three main peaks can be found in the range of 4–6 eV.

As a comparison, we also performed EELS on monolayer graphene and h-BN [dark and light gray lines in Fig. 1(d), respectively]. Notably, the h-BN spectrum shows no peaks below 6 eV, and only a rising edge at 6 eV results from its band gap, which also appears in the h-BN/graphene heterostructure spectra and remains unchanged regardless of the presence of graphene or the twist angle. The graphene spectrum has a single peak at ∼4.75 eV, close to the peaks with the lowest energies in the twisted h-BN/graphene heterostructure spectra, and is labeled as the first transition. The second and third transitions did not appear in the h-BN or graphene monolayer spectrum, but showed up in the h-BN/graphene heterostructure spectra, indicating that the new second and third transitions originate from the interlayer transitions between h-BN and graphene.
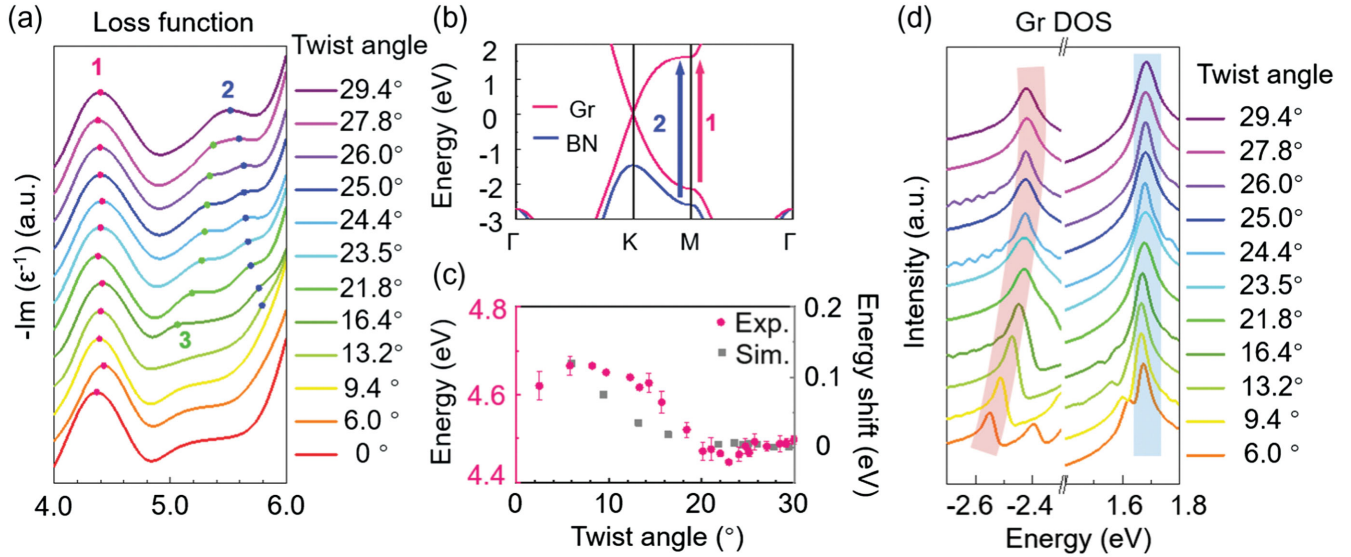
FIG. 2.   Energy loss function and Gr-Gr intralayer transition. (a) Calculated energy loss functions of twisted h-BN/Gr heterostructures. (b) Calculated band structure of h-BN/Gr vertical heterostructure with 0° twist angle, in which the pink and blue arrows indicate the first and the second transition pathways, respectively. (c) Comparison of experimental (pink) and DFT-simulated results (gray) of the Gr-Gr transitions in h-BN/Gr heterostructures with different twist angles. (d) Calculated Gr DOS in h-BN/Gr heterostructure with different twist angles, in which the pink and blue shades cover the ranges of DOS peaks in Gr valence and conduction bands, respectively.

We then used the independent-particle approximation (IPA) [42] to calculate the electron energy loss function (ELF) as the imaginary part of the inverse of the dielectric function $-\mathrm{Im}(\varepsilon^{-1})$ [39], as shown in Fig. 2(a). The heterostructure models used in these simulations are integrated in Table S1 in the Supplemental Material [31]. All three branches of peaks can be found in the calculated ELFs. The first transition energies show rather stable values. The second and third transition energies have inverse tendency as the twist angle increases, and come to the same value near 30°. The third transition appears when twist angles are larger than $\sim$16°. The peak intensities of the second and third transitions are smaller than that of the first transition, and become stronger when twist angles increase. All these features agree well with the experimental results.

Previous studies reported that the excitonic effects can be found in graphene and transition-metal dichalcogenides [43,44]. In our study, considering the transition energy evolutions in experimental results fit very well with the IPA calculations even without considering the excitons' effect [42], the possible excitonic effects should not play a significant role in our case. But further theoretical approaches considering the excitonic effect may lead to more accurate results in simulations.

Earlier studies recognized the peak in graphene at $\sim$5 eV as π plasmons [45,46] because of their dispersive behavior with plasmon feature [40–42]. However, recent work noted that this excitation is actually an interband transition [47] in EELS characterizations. In fact, in typical on-axis EELS experiments with $q = 0$ signal included, the signal with $q \neq 0$ is much weaker than that at $q = 0$,

making the direct transmission electrons, i.e., $q \rightarrow 0$, prominent, while the contribution from the nonzero-momentum-transfer signal is almost negligible (a detailed discussion can be found in the Supplemental Material and Fig. S5 [31]). Moreover, the plasmon disappears when $q = 0$ [41], and the excitation energy approaches the single-particle energy gap [40]. Therefore, the plasmon influence should be very small. The effects of the plasmon are studied experimentally and presented in Figs. S6 and S7 in the Supplemental Material [31]. Considering the large convergence angle in experimental conditions has much better spatial resolution but little influence on the EELS results, we choose large convergence and collection semiangles to avoid the possible effects of carbon contamination in our experiment (see Methods and Fig. S8 in Supplemental Material [31] for details). We will only consider vertical interband transitions hereinafter.

Combined with first-principle calculations, we identified the first and second transitions as the graphene intralayer transition and the interlayer transition from h-BN to graphene [Fig. 2(b), the pink and blue arrows indicate the transition pathways of intralayer and interlayer transitions, respectively]. For these two transitions, the end points are the M point in the graphene conduction band, while the starting points can be attributed to the M point in the valence bands of graphene and a twist-angle-related point in the valence bands of h-BN, respectively [40]. The third transition is caused by other interlayer transition pathways from h-BN to graphene owing to the twist and will be discussed below.

We first studied the evolution of the graphene intralayer transition at the M point with the h-BN interaction. The statistics of all experimental results are shown as pink points in Fig. 2(c). The transition energy decreases by ~ 0.22 eV with the twist angle increasing up to 30°. First-principle calculations were performed to reveal the underlying mechanism of the energy shift. We can pinpoint the transition start and end points by a comparison between the peaks in the calculated ELFs and the energy differences of the density of state (DOS) vHS and correspondent bands. The DOS projected on graphene layers is shown in Fig. 2(d). Two DOS peaks that originate from the graphene vHS at the M point in both the valence band and conduction band, contribute to the response in the EELS spectrum of the graphene intralayer transition. The pink shade marks the variation in the valence vHS of graphene, which is the starting point of intralayer transition and decreases as the twist angle increases. At the same time, the conduction vHS (end point) covered by the blue shade remains unchanged with different twist angles. Therefore, the intralayer transition energy drop is caused by the variation in the valence band of graphene owing to a different moiré potential at the heterointerface. Although the well-known band gap error with the Perdew-Burke-Ernzerhof functional [48,49] makes the simulated transition energies smaller than the experimental results, the tendency of the simulated energy shift [gray squares in Fig. 2(c)] shows excellent agreement with the experimental results.

To further distinguish the origin of the second and third transitions, we compared the calculated ELF results between 26.0° twisted h-BN/graphene heterostructures with (~ 3.4 Å interlayer distance) and without (15 Å interlayer distance) interlayer interaction, as shown in Fig. 3(a). The second and third peaks disappear in the separated structure, suggesting that they correspond to the interlayer transitions between h-BN and graphene.

The energy of the second interlayer transition in the h-BN/graphene heterostructure was extracted and represented as blue points in Fig. 3(b). The transition energy decreases ~ 0.5 eV (from 5.6 to 5.1 eV) as the twist angle increases. Based on the above discussion, this transition occurs between the valence band of h-BN, which varies with the twist angle, and the flat M-point conduction band of graphene. Since the graphene M-point conduction band remains fixed, we only considered the evolution of the transition starting point on the h-BN valence band. The BZ of the twisted system is schematically shown in Fig. 3(c), where the pink and blue hexagons correspond to the BZ for graphene and h-BN, respectively. When the twist angle θ changes, the graphene M point will project onto different positions in the h-BN BZ. In this way, the starting points in the interlayer vertical transitions will form a circular track in the h-BN BZ with a radius of the $\Gamma - M$ reciprocal distance when θ varies from 0° to 360° [indicated by the dark dashed circle in Fig. 3(c)]. We projected the M point of the graphene
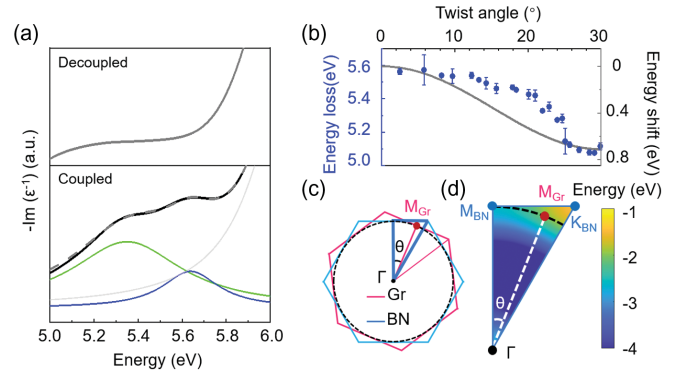

FIG. 3. h-BN/Gr interlayer transition. (a) Comparison between the calculated ELF of 26.0° twisted h-BN/Gr heterostructures with (~ 3.4 Å interlayer distance) and without (15 Å interlayer distance) interlayer interaction. The blue and green lines correspond to the fitted second and third transitions, respectively. The light gray line is the background caused by the h-BN intralayer transition. The dashed gray line is the summed signal. (b) Experimental results (blue points) and DFT-simulated results (gray line) of the transitions with different twist angles. (c) Schematic of the θ twist h-BN/Gr BZ, in which the black dashed circle indicates the track of the Gr M point with all possible twist angles. (d) Valence band energy of h-BN in the Γ-M-K triangle, in which the black dashed line indicates the trace Gr M point projecting on h-BN BZ. Color bar: The relative energy of the h-BN valence band below the Fermi level.

BZ to the superimposed rotated first h-BN BZ, as the red point in Figs. 3(c) and 3(d) indicated. The projected BZ point is located inside the h-BN BZ as shown in Fig. 3(d). Then we pinpoint the corresponding transition starting point on the first valence band of h-BN. As indicated by the black dashed arc in Fig. 3(d), along the graphene M-point projection trace in the h-BN BZ, the valence band energy decreases by approximately 0.8 eV from the M point at 0° to a non-high-symmetry point on the $\Gamma - K$ line at 30°. The energy drop is thus equivalent to the shift of the starting point projected on the h-BN valence band. We tracked the energy shift when the twist angle changes from 0° to 30° [gray line in Fig. 3(b)], and it qualitatively matches the tendency of the experimental results. Note that we have only considered the influence from the evolution of the transition start point based on the same 0° twist structure in this part, while the band difference owing to the twist-angle-dependent moiré potential [13,50] and the contributions from other non-high-symmetry points are ignored (see Supplemental Material Fig. S9 [31]), which contribute to a discrepancy between the experimental results and the calculated energy in Fig. 3(b).

For the third transition appearing at 18°–25°, it comes from other interlayer transition pathways, as evident by Fig. 3(a). Direct transitions on non-high-symmetry points in reciprocal space contribute to the third transition. The transition start and end bands are the same as the second transition. The transition energies of the second and third transitions become the same at large twist angles, leading
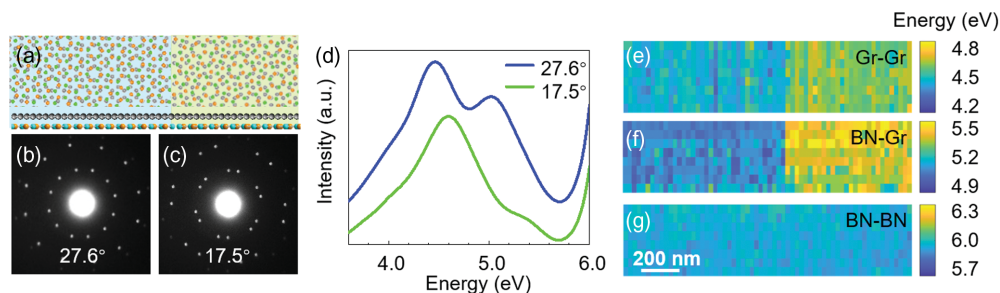
FIG. 4. EELS mapping of the transition energies. (a) Schematic of a 27.6°/17.5° twist h-BN/Gr heterostructure boundary. (b),(c) Diffraction patterns recorded on different sides of the boundary with a twist angle of (b) 27.6° (left) or (c) 17.5° (right). (d) Comparison between the integrated spectra on different sides of the boundary. (e)–(g) Energy mapping of the (e) Gr intralayer transition, (f) h-BN/Gr interlayer transition, and (g) h-BN intralayer transition at the boundary.

to the large peak overlap approaching 30° (a detailed discussion can be found in Supplemental Material and Fig. S9 [31]).

Notably, the difference of the transition energies enables identification of the twist angle by characteristic energies. In our experiment, the graphene we used is whole single crystalline [51], while the h-BN stacked on graphene is actually polycrystalline in micrometer scale [52], which results in some horizontal boundaries between h-BN/graphene heterostructures. Figure 4(a) shows a schematic of a typical horizontal boundary with different twist angles, which are estimated to be 27.6° and 17.5° by diffraction patterns [Figs. 4(b) and 4(c)], but are difficult to distinguish in low-magnification HAADF images. The typical EELS spectra are shown in Fig. 4(d). The graphene intralayer transition energy and h-BN/graphene interlayer transition energy show obvious redshifts of ∼100 and ∼280 meV from 17.5° to 27.6°, respectively, while the band gap of h-BN remains unchanged (evaluated by the rising edge before 6 eV) as the band gap is probably at the K point [53], which has little overlap with the band of graphene. We can clearly distinguish the characteristic energies of the graphene intralayer transition and h-BN/graphene interlayer transition from the extracted energy distributions [Figs. 4(e) and 4(f)], which show sharp contrasts at the boundary. For comparison, the mapping of the h-BN band gap [Fig. 4(g)] does not have any spatial features and remains uniform, indicating an intrinsic feature without influence from the moiré potential.

In conclusion, we studied the twist-angle-dependent intralayer and interlayer transition behavior in h-BN/graphene heterostructures. Owing to the moiré potential, the graphene M-point intralayer transition energy decreases by ∼0.22 eV when the twist angle increases from 0° to 30°. Meanwhile, the flat conduction band at the graphene M point offers a new transition end state for the electrons in the h-BN valence band, making an interlayer transition with an energy even lower than the band gap of h-BN possible. Because the transition starting point changes when graphene twists on h-BN while the end point is fixed at the graphene M point, the transition energy varies from ∼5.6 to ∼5.1 eV when the twist

angle increases from 0° to 30°. Our study revealed that in twisted 2D systems, even heterointerfaces between a wide band gap insulator and a semimetal, such as h-BN and graphene, can contribute to new transition channels with different twist angles. Therefore, we should carefully address each 2D heterointerface to prevent unexpected influence on devices. Additionally, this provides new ways to design advanced 2D optoelectronic devices with artificial wavelengths.

---

* khliu@pku.edu.cn
† p-gao@pku.edu.cn
‡ zhangyuyang@ucas.ac.cn

[1] K. S. Novoselov, A. K. Geim, S. V. Morozov, D. Jiang, Y. Zhang, S. V. Dubonos, I. V. Grigorieva, and A. A. Firsov, Electric field effect in atomically thin carbon films, Science **306**, 666 (2004).

[2] Y. Liu, Y. Huang, and X. Duan, van der Waals integration before and beyond two-dimensional materials, Nature (London) **567**, 323 (2019).

[3] A. K. Geim and I. V. Grigorieva, van der Waals heterostructures, Nature (London) **499**, 419 (2013).

[4] K. S. Novoselov, A. Mishchenko, A. Carvalho, and A. H. Castro Neto, 2D materials and van der Waals heterostructures, Science **353**, aac9439 (2016).

[5] Y. Liu, N. O. Weiss, X. Duan, H.-C. Cheng, Y. Huang, and X. Duan, van der Waals heterostructures and devices, Nat. Rev. Mater. **1**, 16042 (2016).

[6] K. Tang and W. Qi, Moiré-pattern-tuned electronic structures of van der Waals heterostructures, Adv. Funct. Mater. **30,** 2002672 (2020).

[7] Y. Jiang, S. Chen, W. Zheng, B. Zheng, and A. Pan, Interlayer exciton formation, relaxation, and transport in TMD van der Waals heterostructures, Light Sci. Appl. **10,** 72 (2021).

[8] Y.-C. Lin, A. Motoyama, P. Solís-Fernández, R. Matsumoto, H. Ago, and K. Suenaga, Coupling and decoupling of bilayer graphene monitored by electron energy loss spectroscopy, Nano Lett. **21,** 10386 (2021).

[9] J. M. B. Lopes dos Santos, N. M. R. Peres, and A. H. Castro Neto, Graphene Bilayer with a Twist: Electronic Structure, Phys. Rev. Lett. **99,** 256802 (2007).

[10] G. Li, A. Luican, J. M. B. Lopes dos Santos, A. H. Castro Neto, A. Reina, J. Kong, and E. Y. Andrei, Observation of van Hove singularities in twisted graphene layers, Nat. Phys. **6,** 109 (2010).

[11] I. Brihuega, P. Mallet, H. González-Herrero, G. Trambly de Laissardière, M. M. Ugeda, L. Magaud, J. M. Gómez-Rodríguez, F. Ynduráin, and J.-Y. Veuillen, Unraveling the Intrinsic and Robust Nature of van Hove Singularities in Twisted Bilayer Graphene by Scanning Tunneling Microscopy and Theoretical Analysis, Phys. Rev. Lett. **109,** 196802 (2012).

[12] K. Kim, S. Coh, L. Z. Tan, W. Regan, J. M. Yuk, E. Chatterjee, M. F. Crommie, M. L. Cohen, S. G. Louie, and A. Zettl, Raman Spectroscopy Study of Rotated Double-Layer Graphene: Misorientation-Angle Dependence of Electronic Structure, Phys. Rev. Lett. **108,** 246103 (2012).

[13] W. Yan, M. Liu, R.-F. Dou, L. Meng, L. Feng, Z.-D. Chu, Y. Zhang, Z. Liu, J.-C. Nie, and L. He, Angle-Dependent van Hove Singularities in a Slightly Twisted Graphene Bilayer, Phys. Rev. Lett. **109,** 126801 (2012).

[14] Y. Cao, V. Fatemi, S. Fang, K. Watanabe, T. Taniguchi, E. Kaxiras, and P. Jarillo-Herrero, Unconventional superconductivity in magic-angle graphene superlattices, Nature (London) **556,** 43 (2018).

[15] B. Hunt et al., Massive Dirac fermions and Hofstadter butterfly in a van der Waals heterostructure, Science **340,** 1427 (2013).

[16] E. Wang et al., Gaps induced by inversion symmetry breaking and second-generation Dirac cones in graphene/hexagonal boron nitride, Nat. Phys. **12,** 1111 (2016).

[17] C. Jin et al., Observation of moiré excitons in WSe$_2$/WS$_2$ heterostructure superlattices, Nature (London) **567,** 76 (2019).

[18] K. Tran et al., Evidence for moiré excitons in van der Waals heterostructures, Nature (London) **567,** 71 (2019).

[19] N. Ubrig et al., Design of van der Waals interfaces for broad-spectrum optoelectronics, Nat. Mater. **19,** 299 (2020).

[20] S. Lin, High performance graphene/semiconductor van der Waals heterostructure optoelectronic devices, Nano Energy 27 (2017).

[21] C. Su et al., Tuning colour centres at a twisted hexagonal boron nitride interface, Nat. Mater. **21,** 896 (2022).

[22] K. L. Seyler, P. Rivera, H. Yu, N. P. Wilson, E. L. Ray, D. G. Mandrus, J. Yan, W. Yao, and X. Xu, Signatures of moiré-trapped valley excitons in MoSe$_2$/WSe$_2$ heterobilayers, Nature (London) **567,** 66 (2019).

[23] Y. Tang et al., Simulation of Hubbard model physics in WSe$_2$/WS$_2$ moiré superlattices, Nature (London) **579,** 353 (2020).

[24] G. Cassabois, P. Valvin, and B. Gil, Hexagonal boron nitride is an indirect bandgap semiconductor, Nat. Photonics **10,** 262 (2016).

[25] Z. Qiu et al., Giant gate-tunable bandgap renormalization and excitonic effects in a 2D semiconductor, Sci. Adv. **5,** eaaw2347 (2019).

[26] N. O. Weiss, H. Zhou, L. Liao, Y. Liu, S. Jiang, Y. Huang, and X. Duan, Graphene: An emerging electronic material, Adv. Mater. **24,** 5782 (2012).

[27] S.-B. Song et al., Deep-ultraviolet electroluminescence and photocurrent generation in graphene/hBN/graphene heterostructures, Nat. Commun. **12,** 7134 (2021).

[28] Z. Liu, L. H. G. Tizei, Y. Sato, Y.-C. Lin, C.-H. Yeh, P.-W. Chiu, M. Terauchi, S. Iijima, and K. Suenaga, Postsynthesis of h-BN/graphene heterostructures inside a STEM, Small **12,** 252 (2016).

[29] M. Liu, X. Yin, E. Ulin-Avila, B. Geng, T. Zentgraf, L. Ju, F. Wang, and X. Zhang, A graphene-based broadband optical modulator, Nature (London) **474,** 64 (2011).

[30] C. R. Woods et al., Commensurate–incommensurate transition in graphene on hexagonal boron nitride, Nat. Phys. **10,** 451 (2014).

[31] See Supplemental Material at http://link.aps.org/supplemental/10.1103/PhysRevLett.131.016201, which includes Refs. [32–41], for a description of methods, relationship between moiré wavelengths and twist angles, diffraction patterns of h-BN/graphene heterojunctions, comparison between the IPA and RPA results, details of the models used in simulations, the energy shift caused by the h-BN lattice distortion in the DFT calculation, mechanism of the zero-momentum-transfer measurement in EELS, impact of plasmon dispersion in the graphene π signal, a typical example for carbon contamination on graphene, and the energy evolution of the interlayer transition.

[32] G. Kresse and J. Furthmüller, Efficiency of ab-initio total energy calculations for metals and semiconductors using a plane-wave basis set, Comput. Mater. Sci. **6,** 15 (1996).

[33] J. P. Perdew, K. Burke, and M. Ernzerhof, Generalized Gradient Approximation Made Simple, Phys. Rev. Lett. **77,** 3865 (1996).

[34] S. Grimme, J. Antony, S. Ehrlich, and H. Krieg, A consistent and accurate ab initio parametrization of density functional dispersion correction (DFT-D) for the 94 elements H-Pu, J. Chem. Phys. **132,** 154104 (2010).

[35] S. Grimme, S. Ehrlich, and L. Goerigk, Effect of the damping function in dispersion corrected density functional theory, J. Comput. Chem. **32,** 1456 (2011).

[36] M. Gajdoš, K. Hummer, G. Kresse, J. Furthmüller, and F. Bechstedt, Linear optical properties in the projector-augmented wave methodology, Phys. Rev. B **73,** 045112 (2006).

[37] K. Hermann, Periodic overlayers and moiré patterns: Theoretical studies of geometric properties, J. Phys. Condens. Matter **24,** 314210 (2012).

[38] M. M. van Wijk, A. Schuring, M. I. Katsnelson, and A. Fasolino, Moiré Patterns as a Probe of Interplanar Interactions for Graphene on h-BN, Phys. Rev. Lett. **113,** 135504 (2014).

[39] R. F. Egerton, *Electron Energy-Loss Spectroscopy in the Electron Microscope* (Springer Science & Business Media, New York, 2011).

[40] P. Li, X. Ren, and L. He, First-principles calculations and model analysis of plasmon excitations in graphene and graphene/hBN heterostructure, Phys. Rev. B **96**, 165417 (2017).

[41] V. U. Nazarov, Electronic excitations in quasi-2D crystals: What theoretical quantities are relevant to experiment?, New J. Phys. **17**, 073018 (2015).

[42] P. Wachsmuth, R. Hambach, M. K. Kinyanjui, M. Guzzo, G. Benner, and U. Kaiser, High-energy collective electronic excitations in free-standing single-layer graphene, Phys. Rev. B **88**, 075433 (2013).

[43] L. Yang, J. Deslippe, C.-H. Park, M. L. Cohen, and S. G. Louie, Excitonic Effects on the Optical Response of Graphene and Bilayer Graphene, Phys. Rev. Lett. **103**, 186802 (2009).

[44] J. Hong, R. Senga, T. Pichler, and K. Suenaga, Probing Exciton Dispersions of Freestanding Monolayer WSe_2 by Momentum-Resolved Electron Energy-Loss Spectroscopy, Phys. Rev. Lett. **124**, 087401 (2020).

[45] T. Eberlein, U. Bangert, R. R. Nair, R. Jones, M. Gass, A. L. Bleloch, K. S. Novoselov, A. Geim, and P. R. Briddon, Plasmon spectroscopy of free-standing graphene films, Phys. Rev. B **77**, 233406 (2008).

[46] J. Lu, K. P. Loh, H. Huang, W. Chen, and A. T. S. Wee, Plasmon dispersion on epitaxial graphene studied using high-resolution electron energy-loss spectroscopy, Phys. Rev. B **80**, 113410 (2009).

[47] F. J. Nelson, J.-C. Idrobo, J. D. Fite, Z. L. Mišković, S. J. Pennycook, S. T. Pantelides, J. U. Lee, and A. C. Diebold, Electronic excitations in graphene in the 1–50 eV range: The π and $\pi + \sigma$ peaks are not plasmons, Nano Lett. **14**, 3827 (2014).

[48] A. Seidl, A. Görling, P. Vogl, J. A. Majewski, and M. Levy, Generalized Kohn-Sham schemes and the band-gap problem, Phys. Rev. B **53**, 3764 (1996).

[49] M. K. Y. Chan and G. Ceder, Efficient Band Gap Prediction for Solids, Phys. Rev. Lett. **105**, 196403 (2010).

[50] A. Eckmann *et al.*, Raman fingerprint of aligned graphene/h-BN superlattices, Nano Lett. **13**, 5242 (2013).

[51] X. Xu *et al.*, Ultrafast growth of single-crystal graphene assisted by a continuous oxygen supply, Nat. Nanotechnol. **11**, 930 (2016).

[52] L. Wang *et al.*, Epitaxial growth of a 100-square-centimetre single-crystal hexagonal boron nitride monolayer on copper, Nature (London) **570**, 91 (2019).

[53] D. Wickramaratne, L. Weston, and C. G. Van de Walle, Monolayer to bulk properties of hexagonal boron nitride, J. Phys. Chem. C **122**, 25524 (2018).